Fragment merging strategies with known pyrimidine scaffolds targeting dihydrofolate reductase from *Mycobacterium tuberculosis*

Author list: Mr. Tim Kirkman[1]*, Ms. Suk Fun Tan[2]*, Mr. Sair Maximo Chavez Pacheco[3], Dr. Alexander Hammer [2], Prof. Chris Abell[2+], Dr. Manuela Tosin[1], Dr. Anthony G. Coyne[2#], Dr. Marcio V. B. Dias[1,3#]

*equal contributions

#corresponding authors: A.G.C (agc40@cam.ac.uk), M.V.B.C (mvbdias@usp.br and marcio.dias@warwick.ac.uk)

[+] Chris Abell passed away in October 2020

Addresses:

[1] Department of Chemistry, University of Warwick, Gibbet Hill, Coventry CV4 7AL, U.K.

[2] Yusuf Hamied Department of Chemistry, University of Cambridge, Lensfield Road, Cambridge, CB2 1EW, United Kingdom

[3] Department of Microbiology, Institute of Biomedical Science, University of São Paulo. Av. Prof. Lineu Prestes, 1374, CEP 05508-000, São Paulo, SP, Brazil.

Keywords: FBDD, tuberculosis, DHFR, crystallography.

Abstract: Dihydrofolate reductase (DHFR) is a key enzyme involved in the folate pathway that has been heavily targeted for the development of therapeutics against cancer and bacterial and protozoa infections amongst others. Despite being an essential enzyme for *Mycobacterium tuberculosis* (*Mtb*) viability, DHFR remains an underexploited target for tuberculosis (TB) treatment. Herein, we report the preparation and evaluation of a series of compounds against *Mtb* DHFR (*Mtb*DHFR). The compounds have been designed using a merging strategy of traditional pyrimidine-based antifolates with a previously discovered unique fragment hit against *Mtb*DHFR. In this series, four compounds displayed a high affinity against *Mtb*DHFR, with sub-micromolar affinities. Additionally, we determined the binding mode of six of the best compounds using protein crystallography, which revealed occupation of an underutilised region of the active site.

Introduction

Tuberculosis (TB) is an infectious disease that still affects around a third of the world's population, particularly in Africa and South-East Asia. TB is caused by *Mtb* and is the highest cause of death from a single infectious agent, although this title was temporarily lost at the height of the COVID-19 pandemic, with an estimated 1.4 million deaths in 2021.[1] Of particular concern is the emergence of multi-drug resistance (MDR), which involves resistance to isoniazid and rifampicin, the two most commonly used drugs against TB. MDR TB strains greatly increase treatment cost, regime duration, and treatment failure possibilities. For these reasons, the development of new treatment options with novel modes of action to combat this disease is urgently needed.[2]

Dihydrofolate reductase (DHFR) is a key enzyme for the biosynthesis of tetrahydrofolate (THF), which is involved in a variety of critical cellular processes. THF is vital for *de novo* biosynthesis of purines, various amino acids, and thymine.[3] DHFR is a well-established target for an array of diseases, with drugs that target DHFR being used as antibacterial, antifungal, antimalarial, and anticancer agents.[4] The drugs used as antimicrobials are distinct from those used as anticancer because of their specificity to the enzyme active site.[5] Trimethoprim (TMP) and pyrimethamine (PYR) are antifolates used for

bacterial and malaria infections, respectively (Figure 1).[6] Although in *Mtb*, it has been shown that inhibition of the folate pathway leads to cell death,[7] currently DHFR inhibitors are unsuitable for TB treatment due to lack of selectivity, inability to penetrate the mycobacterial cell wall, or low affinity for *Mtb*DHFR.[8] DHFR can still be considered a potential drug target for *Mtb*, however it requires the development of new molecules to inhibit its activity. Such molecules can be discovered using different strategies, including fragment-based drug discovery (FBDD) approaches.

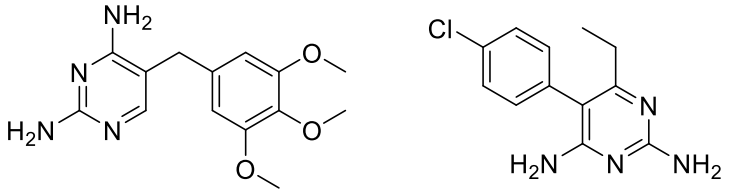

Trimethoprim (**1**) Pyrimethamine (**2**)

Figure 1 – Chemical structures of trimethoprim (TMP, left) and of pyrimethamine (PYR, right).

Fragment-based approaches rely on a strategy in which high-affinity compounds are developed starting from low complexity fragments, typically weighing less than 300 Da, and assessing them *via* various biophysical methods.[9] Starting from small chemical compounds (fragments), precise occupation of the desired region can be achieved through fragment merging, linking, and growing.[10],[11] Through FBDD, different companies have already generated over 40 new drugs that entered clinical trials, with six of them being approved for clinical use.[12]

In a previous work carried out by our research groups, an FBDD approach was applied to *Mtb*DHFR.[13] Based on a fragment screening campaign that utilised a range of biophysical methods, including differential scanning fluorometry, nuclear magnetic resonance, and isothermal titration calorimetry, we confirmed the binding of twenty-one fragments, and we obtained X-ray crystal structures of *Mtb*DHFR in complex with nine of them. Several of these fragment hits provided potential starting points for fragment elaboration attempts, with a particular interest towards fragment **5** (Figure 2). Two molecules of **5** were observed to bind independent of each other to the *Mtb*DHFR substrate binding region. One of these was found to occupy a unique region adjacent to the binding region of traditional antifolates, known as the glycerol-binding pocket (GBP, orange region in Figure 2).[14] This region is a unique area when compared to the human analogue of DHFR, being hydrophobic for the human equivalent and hydrophilic for *Mtb*DHFR , and substantially smaller in the human analogue. It is named GBP since the first structure reported of *Mtb*DHFR, a molecule of glycerol from the cryogenic protecting solution is bound in this cavity.[14] Consequently, targeting this region could allow the development of a novel series of high affinity compounds for *Mtb*DHFR inhibition.

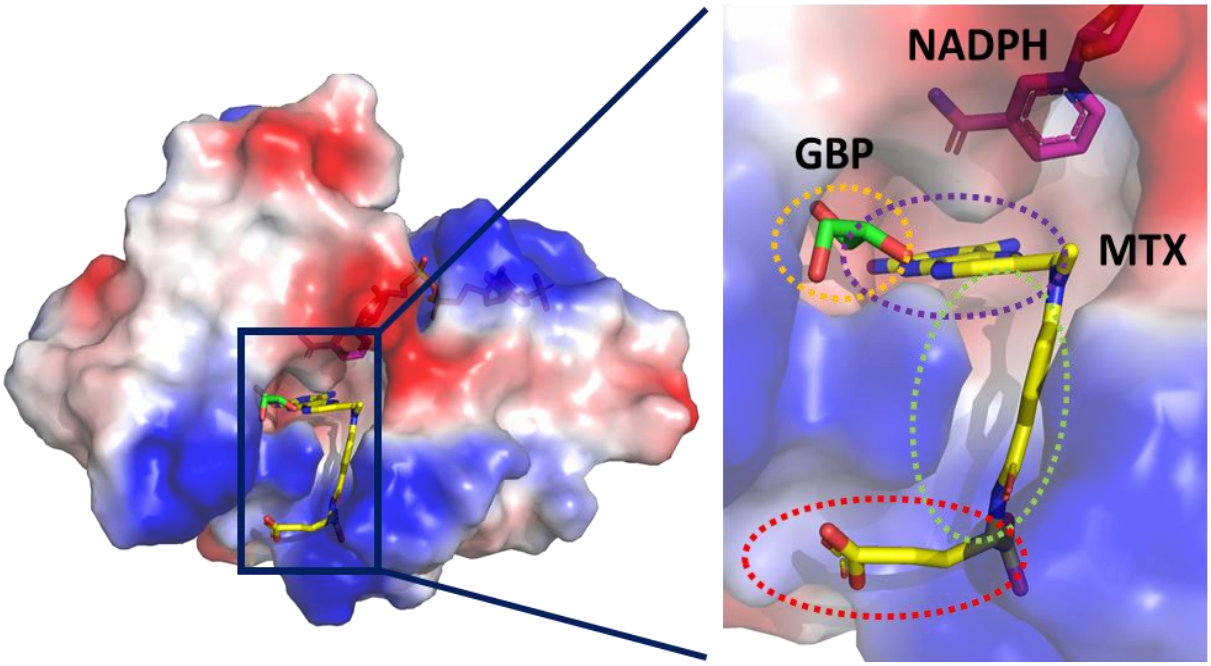

Figure 2 – (left) electrostatic surface of *Mtb* DHFR with NADPH (purple), methotrexate (yellow), and glycerol (green). Electrostatic surface bar included showing red regions are of negative charge and blue of positive. (right) *Mtb* DHFR active site displaying four main regions: Purple – negatively charged region classically occupied by pyrimidine scaffolds. Green – apolar region classically occupied by PABA moiety. Red – positively charged region classically occupied by glutamate moiety. Orange – glycerol binding pocket (GBP), a unique pocket compared to the human analogue.

Hajian *et al*. have reported that a series of propargyl-linked antifolates that have good activity *in vitro* and *in vivo* against *Mtb*.[15] These compounds (such as **3**, Figure 3), were observed to inhibit *Mtb*DHFR and were synthesised based on a pyrimidine scaffold. In a superposition of a crystal structure obtained with a propargyl-linked antifolate and **5**, it can be observed that the pyrazole and pyrimidine rings are in close proximity in different regions of the active site (Figure 3b).

In this work, we hypothesised that merging the pyrazole ring identified from the fragment-based approach from **5** and the pyrimidine ring from known antifolate structures such as **3**, would lead to high affinity compounds for *Mtb*DHFR, expanding into an unexplored region for current DHFR antifolates (Figure 3a). This combination would still allow for the traditional hydrogen-bonding interaction of various residues with the amines in the pyrimidine ring and hydrophobic with the alkynyl and R group associated, but also allow expansion into the GBP for novel interactions (Figure 3b).

Thus, in this work, we carried out a fragment elaboration strategy based on **5**. Based on that, we have obtained compounds with up to +9.3 °C thermal shift against *Mtb*DHFR and K_D of 0.47 µM, a sizable improvement from **5**, with a thermal shift of +1.2 °C and K_D of 640 µM. Additionally, we have obtained the binding mode of these compounds through protein crystallography of *Mtb*DHFR in complex with NADPH and a variety of pyrimidine derived compounds which indicates that these compounds bind to the GBP.

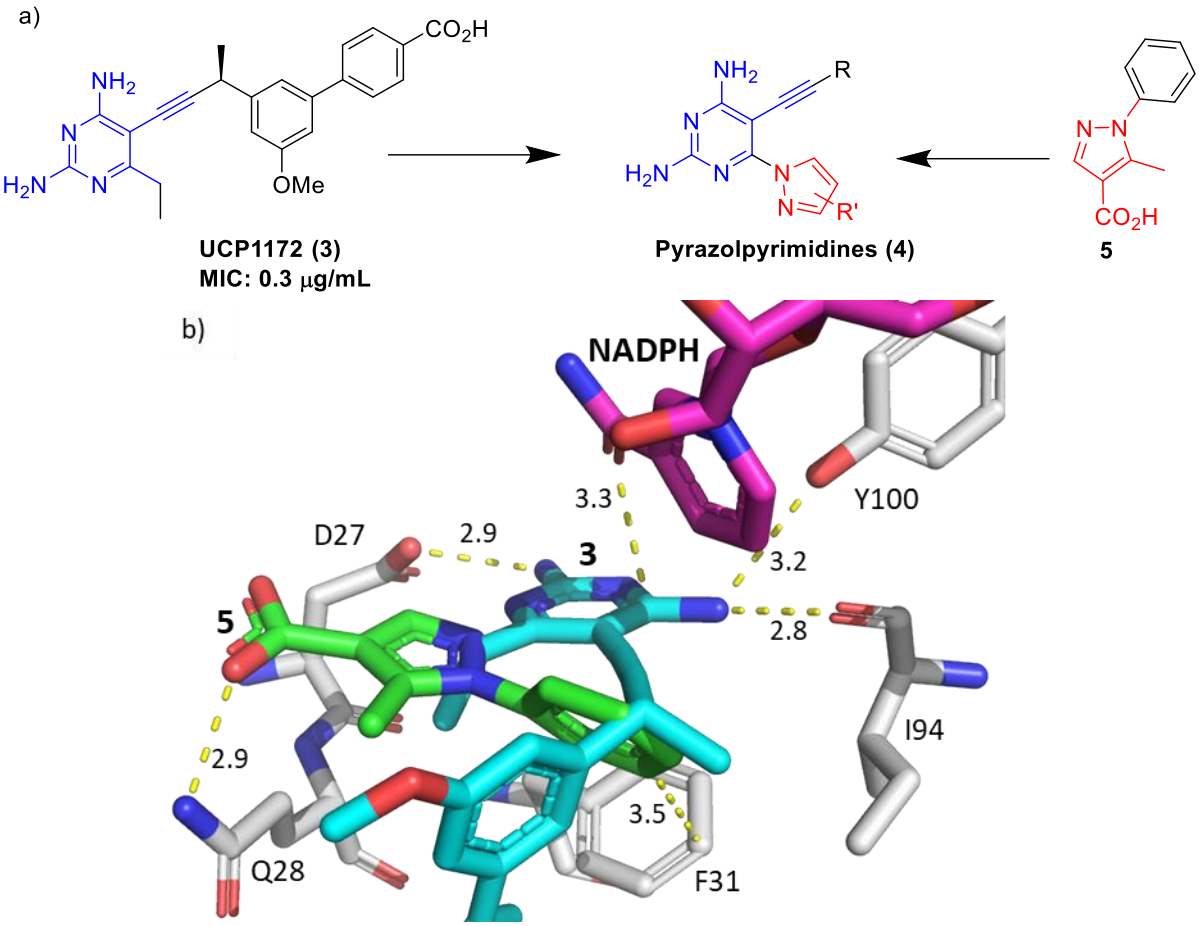

Figure 3 – a) Merging of a fragment previously discovered within the group (**5**) and a known inhibitor (**3**) to form a pyrazolpyrimidine (**4**). b) Overlap of crystal structure of **5** (green) in *MtbDHFR* (white, NADPH in pink, PDB: 6VS5) overlapped with crystal structure of a propargyl-linked antifolate in *MtbDHFR* (PDB: 6DDP, cyan).[15]

Results and Discussion

Synthesis strategy

The majority of compounds were synthesised from 2,6-diamino-4-chloropyrimidine (**6**), which was iodinated using *N*-iodosuccinimide, affording compound **7** (Scheme 1) (Supplementary Methods 2). Through a Sonogashira coupling, a cyclopropylacetylene (**34**) was introduced in place of iodine in ortho to the chlorine. Suzuki couplings with aryl boronic acids carried out on compound **8** then allowed to generate a variety of substituted pyrimidines (**9**-**25**). Sonogashira coupling with cyclopentylacetylene (**34**) and cyclophenylacetylene (**35**) were also performed giving compounds **28** and **29** respectively, with subsequent Suzuki coupling leading to compounds **30**-**33** (Scheme 2b). For **26** and **27** no iodination and subsequent Sonogashira coupling occurred, and only a Suzuki coupling at the chloro position could be performed (Scheme 2a). **8**, **28**, and **29** were taken forward without the subsequent Suzuki coupling, with the chlorine atom remaining part of the compound.

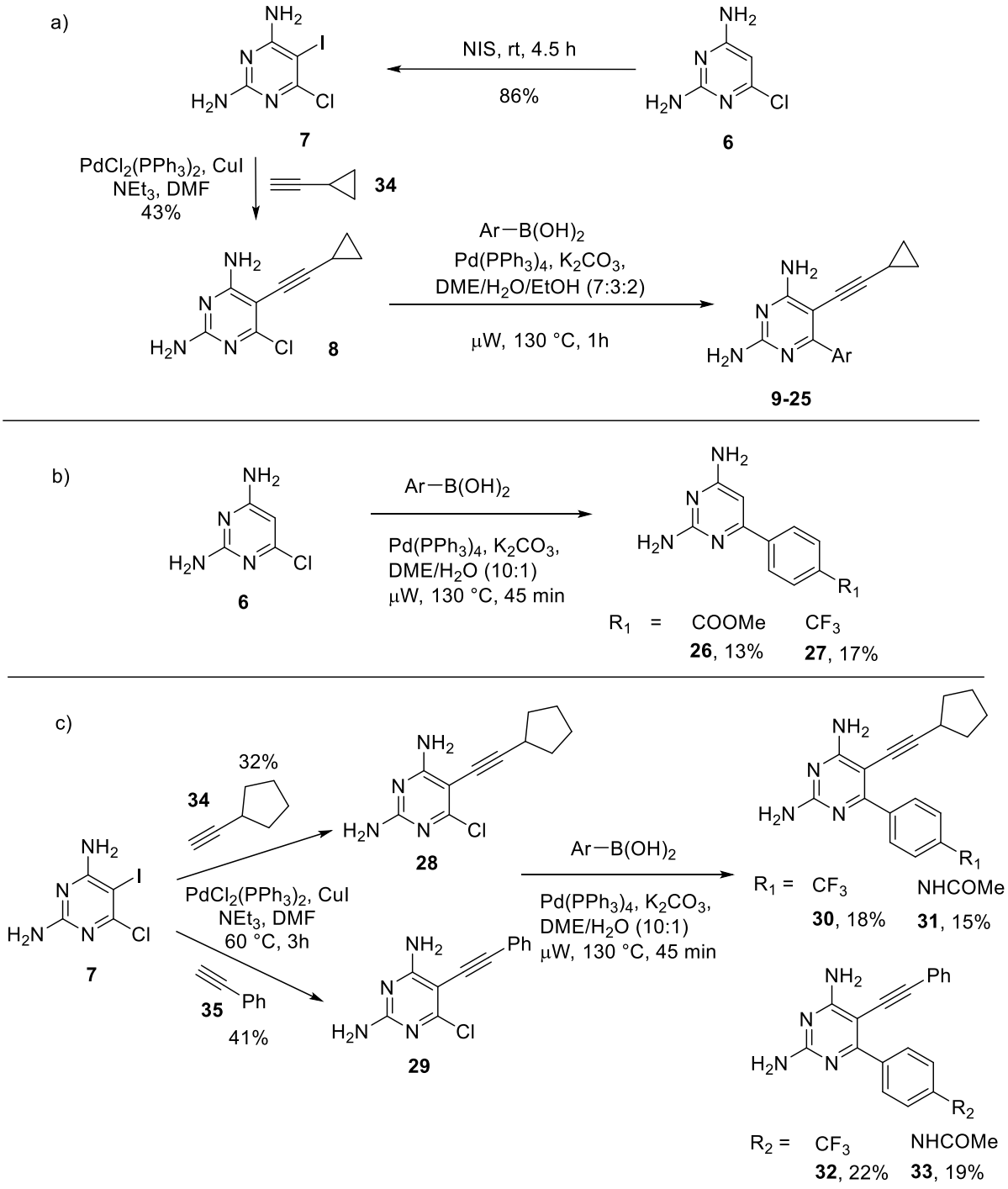

Scheme 1 - Synthetic scheme for compounds a) **6** to **25**, b) **26**-**27** and c) **28**-**33**.

Table 1 - Compounds obtained by Suzuki coupling of aryl boronic acids to **8**

Ar group	Yield (%)	Ar group	Yield (%)	Ar group	Yield (%)
9 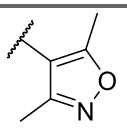	25	**10** 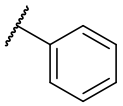	12	**11** 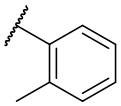	13
12 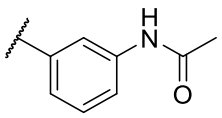	27	**13** 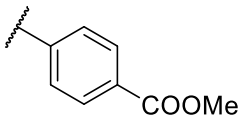	28	**14** 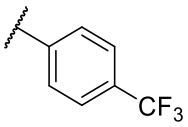	20
15 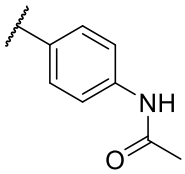	33	**16** 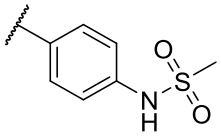	33	**17** 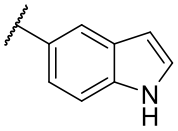	56
18 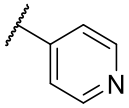	13	**19** 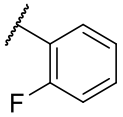	18	**20** 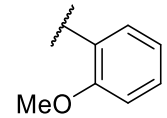	54
21 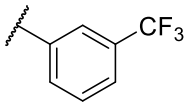	46	**22** 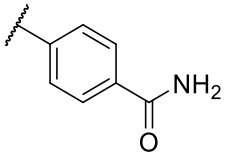	22	**23** 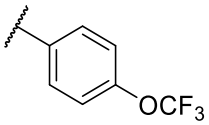	52
24 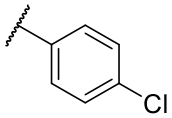	15	**25** 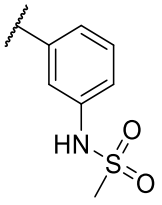	29		

With this series of compounds synthesised (Supplementary Methods 3), characterisation of the interactions and affinity with *Mtb*DHFR with differential scanning fluorimetry (DSF), monitoring thermal shifts, utilised as an initial assay (Table 2).

The isoxazolpyrimidine derivative **9** showed a substantial increase in thermal shift compared to the original fragment **5**, from +1.5 °C to +4.5 °C (Table 2). No thermal shift was observed when the isoxazole ring was removed (compound **8**), showing the importance of an aromatic group in this position for affinity. Removal of the cyclopropyl group (**26** and **27**) also lead to no thermal shift, suggesting occupation of the lipophilic region adjacent to NADPH in conjunction with the GBP is required for affinity. The replacement of isoxazole with the phenyl moiety, **10**, led to further increased thermal shift, from +4.5 °C to +6.0 °C, allowing a wider range of derivatisation due to commercially available phenyl substituents to be explored without worry of lost affinity from this ring alteration.

Table 2 - Thermal shift (TS) data and Isothermal titration calorimetry (ITC) data obtained from the initial compounds synthesised.

Compounds	**Structural modification**	***Mtb*DHFR (0.5 mM) TS (°C)**	***Mtb*DHFR K_D**
5	-	+1.2	640 ±120 µM
8	No Ar	+0.0	--
9	isoxazole	+4.5	3.9 ±1.20 µM
10	Phenyl	+6.0	[a]
11	***o*-Me**	**+9.0**	**2.40 ±0.81 µM**
12	*m*-NHCOMe	+7.0	0.87 ±0.17 µM
13	*p*-COOMe	+7.6	[a]
14	*p*-CF_3	+7.5	0.62 ±0.12 µM
15	*p*-NHCOMe	+7.6	0.76 ±0.20 µM
16	***p*-$NHSO_2$Me**	**+9.3**	**0.47 ±0.14 µM**
17	5-indole	+6.3	[a]
18	pyridine	+4.0	--
19	*o*-F	+5.1	--
20	*o*-OMe	+4.4	[a]
21	*m*-CF_3	+4.5	[a]
22	*p*-$CONH_2$	+4.5	[a]
23	*p*-OCF_3	+3.0	--
24	*p*-Cl	+5.8	[a]
25	***m*-$NHSO_2$Me**	**+8.5**	[a]
26	No propargyl, *p*-COOMe	+0.0	--
27	No propargyl, *p*-CF_3	+0.0	--
28	No Ar, cyclopentane	-1.5	--
29	No Ar, Phenyl	-0.5	--
30	Cyclopentane, *p*-CF_3	+1.5	--
31	**Cyclopentane, *p*-NHCOMe**	**+8.5**	[a]
32	Phenyl, *p*-CF_3	-0.5	--
33	Phenyl, *p*-NHCOMe	+1.5	--

[a] the ITC was measured for these compounds however they showed weak heats of binding and an accurate Kd was not obtained.

A lightly electron donating methyl substituent in the *ortho* position was tolerated, with **11** increasing the thermal shift from +6.0 °C of the unsubstituted phenyl **10**, to +9.0 °C. Other groups synthesised, such as F and OMe for **19** and **20** respectively, appeared to destabilise interactions reducing the thermal shift to +5.1 °C and +4.4 °C respectively.

Meta substitution of the aromatic ring with larger functional groups, such as -NHCOMe for **12** and -$NHSO_2Me$ for **25**, appeared favourable, leading to increases in thermal shift to 7.0 °C and 8.5 °C respectively. At the same *meta* position, the smaller group -CF_3 of **21** appeared to destabilise *Mtb*DHFR binding, reducing the shift from +6.0 °C in the unsubstituted compound **10**, to +4.5 °C. In the *para* position, larger functional groups again seemed most suited for increasing affinity. **13**, **15**, and **16** all showed an increase of thermal shift, particularly **16** increasing to +9.3 °C, the highest increase in thermal shift obtained. Interestingly, the functional group for **16**, -$NHSO_2Me$, is the same for the strongest *meta* substituent tried **25**, highlighting this functional group as one of interest within the GBP. Decreases in thermal shift from **10** were observed for some smaller substituents in the para position: **22**, **23**, and **24**. Compound **14** bucked this trend, being a smaller functional group tried but leading to an increased thermal shift to +7.5 °C.

Replacement of the aromatic ring was also undertaken, with the change to a 5-substituted indole (**17**) leading to a small increase of thermal shift to +6.3 °C, and the change to a pyridine ring (**18**) leading to a reduction to +4.0 °C. This reduction for **18** may be due to the reduced hydrophobic nature of the ring, leading to a more hydrophilic moiety in a hydrophobic region.

Replacement of the cyclopropyl group was also examined, using the same substitution in the GBP as for **14** and **15**. Changes to *p*-CF_3 (**14**) lead to a complete loss of thermal shift gain, changing to +1.5 °C and -0.5 °C for the cyclopentyl and phenyl, respectively. Changes to *p*-NHCOMe (**15**) lead to a decrease to +1.5 C when substituted with a phenyl ring, but surprisingly when substituted to a cyclopentyl for **31**, an increase was observed to +8.5 °C. This is a 0.9 °C increase in shift compared to the cyclopropyl compound **15**. It could be reasoned that the larger size of the cyclopentyl moiety occupies the region more fully than cyclopropyl, and the phenyl has limited affinity due to its size or aromaticity, although it is unclear why a substantial reduction is then observed for **30**. Removal of the GBP portion of the compound for **28** and **29** led to no affinity for *Mtb*DHFR.

Beside TSA assays, ITC was also performed for a number of the synthesised compounds (Supplementary Table 1). As a starting point **9** was assessed, giving a K_D of 3.9 ±1.2 μM, a significant increase from the starting fragment **5** of 640 ±120 μM. **11** exhibited a slight increase in the affinity compared to **9**, with a K_D value of 2.4 ±0.8 μM. It is interesting that the thermal shift observed for this compound (+9.0 C) was the second highest in the series. Despite exhibiting slightly lower thermal shift increases, compounds **12**, **14**, and **15** displayed stronger affinity to *Mtb*DHFR than **11**, with K_Ds of 0.87 ±0.17 μM, 0.62 ±0.12 μM, and 0.76 ±0.20 μM respectively. The compound with the largest thermal shift of the series, **16**, also displayed a K_D value of 0.47 ±0.14 μM. Consequently, this is the compound with the highest affinity synthesized in these series, which an increase of 1000 times from the initial fragment **5**, with a K_D of 640 ±120 μM.[13] The affinity of the compounds discussed above were measured using ITC and these showed good heats of binding. However, for a number of compounds (see Table 1), the heats of binding were poor and accurate affinities for these were not obtained.

To obtain insights into the interactions of molecules from these series with *Mtb*DHFR, co-crystallisation or soaking experiments of compounds with *Mtb*DHFR was undertaken (Supplementary Table 2) . The protein complexes for **14**, **15**, **16**, and **25** were obtained (Figure 4). In all four, it was observed that the pyrimidine-cyclopropane moieties remain in the same position (Figure S1), with the pyrimidine interacting through hydrogen bonding with T113, D27, I5, I94, and Y100 and the

cyclopropane occupying the more hydrophobic region near I94. The acetamide group of **14** interacts with R23 in the GBP through hydrogen bonding, but no interaction with Gln28 (Figure 4a). The trifluoro group of **15** is in closer contact with the Q28 but losing any interaction with the Arg23 (Figure 4b). The sulphonamide of **16**, instead**,** forms tighter hydrogen bonds with both R23 and Q28, with both bonds being under 3Å (Figure 4c). These interactions, along with a greater occupation of space due to the larger functional group size, may explain the greater affinity displayed by **16** compared to the compounds with crystal structures obtained. **25** does not directly interact with either R23 or Q28. However, the sulphonamide group of this compound indirectly interacts through a water molecule with R23 (Figure 4d). In addition, the methyl group of the sulphonamide is in close proximity to the cyclopropane group, experiencing London dispersion forces between them. Crystal structures of **13**, **19**, and **20** were also obtained, with a binding position similar to others obtained, although less hydrogen bonding interactions within the GBP were observed, possibly explaining their weaker affinity (Figure S2).

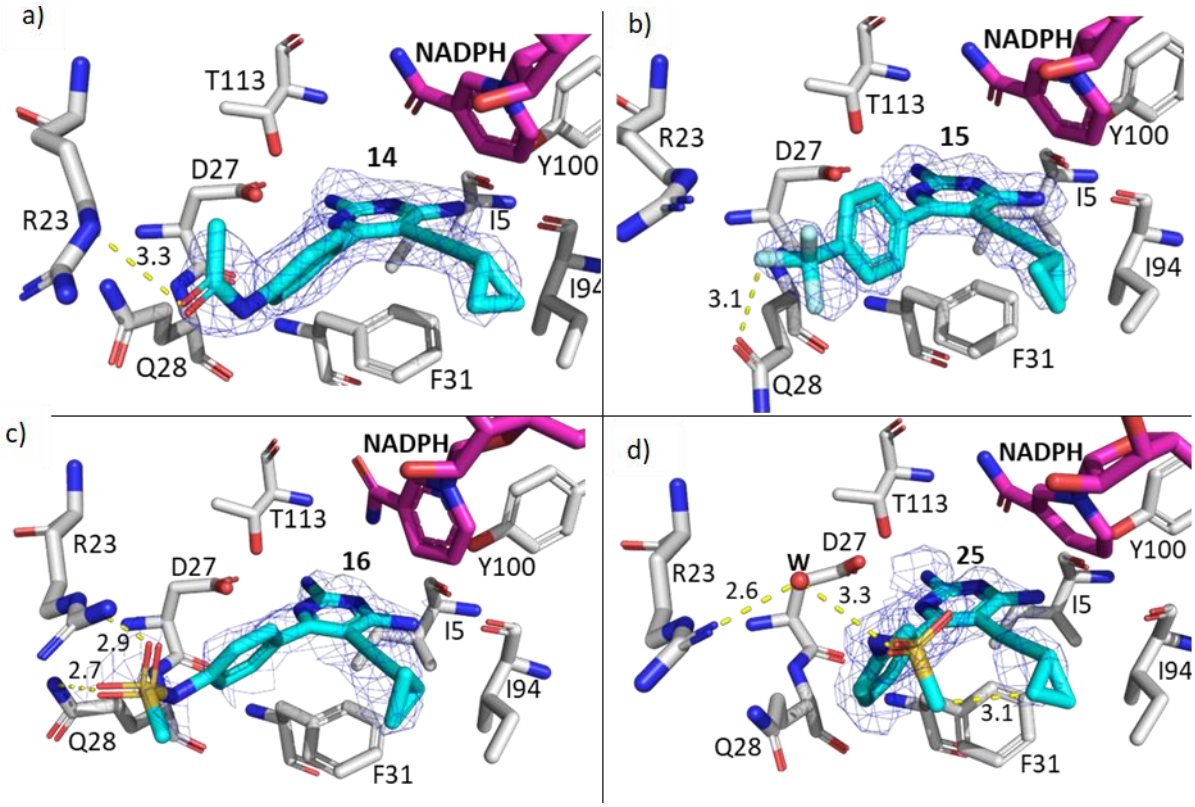

*Figure 4 – Crystal structure of MtbDHFR in complex with NADPH and ligands. a) MtbDHFR (white) in complex with NADPH (pink) and **14** (cyan) with electron density of **14** displayed (PDB: 8CQA). b) MtbDHFR (white) in complex with NADPH (pink) and **15** (cyan) with electron density of **15** displayed (PDB: 8CQ9). c) MtbDHFR (white) in complex with NADPH (pink) and **16** (cyan) with electron density of **16** displayed (PDB: 8COP). b) MtbDHFR (white) in complex with NADPH (pink) and **25** (cyan) with electron density of **25** displayed (PDB: 8COX). All the electron density contours are from 2Fo-Fc maps.*

Amongst the compounds tested, **14**, **15**, and **16** displayed a sizable increase in thermal shift, along with sub-micromolar K_D values, with increases over 1000-fold in relation to the original fragment **5**. In addition, **25** and **33** displayed strong thermal shift increases. Interestingly, compounds **16** and **25** contain the sulphonamide moiety, at the *para* and *meta* position respectively, interacting in the GBP (Figure S3). Bar the initial fragment **5**, this is the first series of compounds confirmed to interact with the *Mtb*DHFR active site and occupy the GBP. A number of these compounds were screened against *Mtb* (H37Rv) (Supplementary Methods 1) however they showed MIC >50 μM (Supplementary Table 3) and further optimisation is needed to improve the mycobacterial cell wall permeability.

Conclusion

In conclusion, combining fragment **5**, discovered from a previous fragment screen within our research group, and structural moieties from classical antifolates, 27 compounds were synthesised as part of a new series to assess the occupation of the previously unexplored and unique GBP region within *Mtb*DHFR. Through TSA and ITC, 3 compounds were determined to be strong candidates for *Mtb*DHFR inhibition, exhibiting sub-micromolar affinity, along with the crystal structure confirming their position in the active site and occupation of the GBP.

Table of contents entry

Tuberculosis, caused by *Mycobacterium tuberculosis* (*Mtb*), remains a major global health problem, with rising resistance increasing the need for more therapeutic options. Through the use of fragment-based drug discovery, a compound found from screening was merged with known inhibitors, creating compounds with sub-micromolar affinity against *Mtb* dihydrofolate reductase, an essential enzyme for *Mtb*.

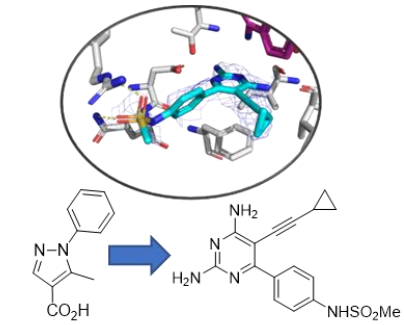

Experimental

*Mtb*DHFR expression and purification

For non-crystallisation characterisation, *Mtb*DHFR was prepared according to the protocol established by Dias *et al*.[16] For crystallisation experiments, a histidine-tag free *Mtb*DHFR was prepared as reported by Ribeiro *et al*.[17] For purification of the histidine-tag free *Mtb*DHFR, the supernatant was loaded onto a methotrexate-agarose column and washed with 3 column volumes (CVs) of phosphate buffer (20 mM K_2HPO_4, 50 mM KCl, pH = 7.5). The protein was eluted with 3 CVs of elution buffer (20 mM K_2HPO_4, 50 mM KCl, DHF 2mM, pH = 7.5). The eluted fraction was dialysed against phosphate buffer. The fraction was further purified using an Superdex 200 16/60 gel filtration chromatography column previously equilibrated with phosphate buffer. Fractions deemed to contain *Mtb*DHFR based on SDS-PAGE analysis were pooled, concentrated at 15 mg/mL and flash frozen in liquid nitrogen and stored at -80°C. The purity of the sample was monitored by SDS-PAGE 12%.

Differential Scanning Fluorimetry (DSF)

The thermal shift assays (TSA) were performed with a CFX Connect™ instrument (BioRad) using 96-well plates. Each well contained 3 mM of DHFR, 1 mM of NADPH, 5 X SYPRO Orange and 0.5 mM or 1mM of compounds, with a final concentration of 20 mM phosphate buffer, 50 mM KCl at pH 7.0. The final DMSO concentration in each well was 5% v/v. The plate was centrifuged prior to the experiment at 1500 rpm for 1 min. The temperature was increased at a constant rate of 0.5 °C/min from 25 to 95 °C. The data in the format of Microsoft Excel were analysed by plotting fluorescence intensity versus the temperature (in °C). Minima of the first derivative of the curve can be used to find the melting temperature ™. The difference in the T_m in the presence and absence of the compounds are defined as thermal shift (DTm).

Isothermal Titration Calorimetry (ITC)

ITC experiments were conducted on a MicroCal auto-iTC200 instrument (Malvern Instruments). All the experiments were performed in the presence of 1mM of NADPH and in the buffer containing 20 mM phosphate (pH 7.0) and 50 mM KCl. The volume of DMSO (from 3 to 7 %) used was dependent on the solubility of the ligands. *Mtb*DHFR concentration of 40 mM and ligand solutions concentrations of 500 mM were used. Typically, ligand solution was titrated to the protein solution over 19 injections with a time intervals of 200 seconds duration; initial titration of 0.4 µL (discarded during data processing), followed by successive 19 x 2 µL titration. Control experiment was performed in the absence of protein and the heat was subtracted from ligand to protein titrations. The data were analysed using Origin Analysis software, by fitting the values to a one-site binding model.

*Mtb*DHFR crystallization and structure determination

All crystallisation experiments were performed by hanging drop vapour diffusion method as described by Ribeiro *et al*.[17]. The protein solution consisted of 10 mg/mL *Mtb*DHFR, and 10 mM NADPH. Briefly, 1 µL of Tag-free *Mtb*DHFR at 10 mg/mL, previously incubated with 2 mM of NADPH, was mixed in a coverslip with 1 µL of a crystallisation condition constituted of 1.6 M ammonium sulfate, 100 mM MES (2-(*N*-morpholino)ethanesulfonic acid), pH 6.5, 10 mM $CoCl_2$ and inverted down against the 1000 µL of crystallisation solution added in the wells of Linbro plate (Hampton Research) and bipyramidal crystal of *Mtb*DHFR appeared after 3-4 days at 20 °C. Ternary complexes of *Mtb*DHFR with different compounds were obtained by co-crystallisation or soaking as described in the Table S2. The co-crystallisation attempts contained 1.5 mM compound of interest with the follow variation in each well, ratios of 1:1, 1:2, and 2:1 of protein and precipitant. For the soaking experiments, 10-20 mM of

compounds dissolved in DMSO were individually added to drops with *Mtb*DHFR crystals in complex with NADPH. Co-crystals or soaked crystals were flash freezing using a cryogenic solution containing 20% glycerol using liquid nitrogen.

The X-ray data collection was performed at Diamond Light Source (UK), PETRA-III (Germany) or LNLS (Brazil). The data was processed by XDS and scaled by Aimless from CCP4i suite.[18–20] The structures were solved by molecular replacement using Phaser MR from Phenix crystallographic suite and the PDB entry 6VS5 as a search model.[21,22] The crystallographic refinement was performed using Phenix.Refine followed by manual inspection using COOT.[23,24] The quality of the models were checked by MolProbity.[25] The figures from the crystal structures were prepared using PyMol.[26]

Acknowledgements

T.K would like to acknowledge the EPRSC for support for a Ph.D studentship. A.H. would like to acknowledge DAAD, Cambridge Trust and Emmanuel College, Cambridge for funding. S.F.T would like to thank the Ministry of Education, Malaysia for funding. SMC-P would like to thank FAPESP (process nº 2017/25733-1) for the TT3 fellowship. This project was funded by FAPESP grant numbers 2015/09188-8, 2018/0351-1, and 2020/03850-9 to MVBD. MVBD also would like to acknowledge the Department of Chemistry from the University of Warwick for research financial support and to CNPq (process number 208998/2020-0) for the productivity in research fellowship. The authors would also like to thank Dr Helena Boshoff (NIH Bethesda) for the screening of compounds against *Mtb* (H37Rv).

References

[1] World Health Organization, *Global Tuberculosis Report 2022*, Geneva, **2022**.

[2] L. Barthod, J. G. Lopez, C. Curti, C. Bornet, M. Roche, M. Montana, P. Vanelle, *J. Chemother.* **2018**, *30*, 1–15.

[3] M. V. Raimondi, O. Randazzo, M. La Franca, G. Barone, E. Vignoni, D. Rossi, S. Collina, *Molecules* **2019**, *24*, DOI 10.3390/molecules24061140.

[4] M. Sharma, P. M. S. Chauhan, *Future Med. Chem.* **2012**, *4*, 1335–1365.

[5] S. Bobone, L. Stella, *Adv. Exp. Med. Biol.* **2019**, *1117*, 175–214.

[6] J. K. Iyer, W. K. Milhous, J. F. Cortese, J. G. Kublin, C. V. Plowe, *Lancet* **2001**, *358*, 1066–1067.

[7] M. R. Nixon, K. W. Saionz, M. S. Koo, M. J. Szymonifka, H. Jung, J. P. Roberts, M. Nandakumar, A. Kumar, R. Liao, T. Rustad, J. C. Sacchettini, K. Y. Rhee, J. S. Freundlich, D. R. Sherman, *Chem. Biol.* **2014**, *21*, 819–830.

[8] B. Hajian, E. Scocchera, C. Shoen, J. Krucinska, K. Viswanathan, N. G-Dayanandan, H. Erlandsen, A. Estrada, K. Mikušová, J. Korduláková, M. Cynamon, D. Wright, *Cell Chem. Biol.* **2019**, *26*, 781-791.e6.

[9] P. Kirsch, A. M. Hartman, A. K. H. Hirsch, M. Empting, *Molecules* **2019**, *24*, DOI 10.3390/MOLECULES24234309.

[10] H. L. Silvestre, T. L. Blundell, C. Abell, A. Ciulli, *Proc. Natl. Acad. Sci. U. S. A.* **2013**, *110*, 12984–12989.

[11] A. W. Hung, H. L. Silvestre, S. Wen, A. Ciulli, T. L. Blundell, C. Abell, *Angew. Chemie Int. Ed.* **2009**, *48*, 8452–8456.

[12] C. Marchetti, D. S. H. Chan, A. G. Coyne, C. Abell, *Parasitology* **2018**, *145*, 184–195.

[13] J. A. Ribeiro, A. Hammer, G. A. Libreros-Zúñiga, S. M. Chavez-Pacheco, P. Tyrakis, G. S. De Oliveira, T. Kirkman, J. El Bakali, S. A. Rocco, M. L. Sforça, R. Parise-Filho, A. G. Coyne, T. L. Blundell, C. Abell, M. V. B. Dias, *ACS Infect. Dis.* **2020**, *6*, 2192–2201.

[14] R. Li, R. Sirawaraporn, P. Chitnumsub, W. Sirawaraporn, J. Wooden, F. Athappilly, S. Turley, W. G. J. Hol, *J. Mol. Biol.* **2000**, *295*, 307–323.

[15] B. Hajian, E. Scocchera, C. Shoen, J. Kordulá, M. Cynamon, D. W. Correspondence, *Cell Chem. Biol.* **2019**, *26*, 781–791.

[16] M. V. B. Dias, P. Tyrakis, R. R. Domingues, A. F. P. Leme, T. L. Blundell, *Structure* **2014**, *22*, 94–103.

[17] J. A. Ribeiro, S. M. Chavez-Pacheco, G. S. de Oliveira, C. dos S. Silva, J. H. P. Giudice, G. A. Libreros-Zúñiga, M. V. B. Dias, *Acta Crystallogr. Sect. D Struct. Biol.* **2019**, *75*, 682–693.

[18] W. Kabsch, *Acta Crystallogr. D. Biol. Crystallogr.* **2010**, *66*, 125–132.

[19] P. R. Evans, G. N. Murshudov, *Acta Crystallogr. D. Biol. Crystallogr.* **2013**, *69*, 1204–1214.

[20] M. D. Winn, C. C. Ballard, K. D. Cowtan, E. J. Dodson, P. Emsley, P. R. Evans, R. M. Keegan, E. B. Krissinel, A. G. W. Leslie, A. McCoy, S. J. McNicholas, G. N. Murshudov, N. S. Pannu, E. A. Potterton, H. R. Powell, R. J. Read, A. Vagin, K. S. Wilson, *Acta Crystallogr. Sect. D* **2011**, *67*,

235–242.

[21] A. J. McCoy, *Acta Crystallogr. D. Biol. Crystallogr.* **2007**, *63*, 32–41.

[22] D. Liebschner, P. V Afonine, M. L. Baker, G. Bunkóczi, V. B. Chen, T. I. Croll, B. Hintze, L.-W. Hung, S. Jain, A. J. McCoy, N. W. Moriarty, R. D. Oeffner, B. K. Poon, M. G. Prisant, R. J. Read, J. S. Richardson, D. C. Richardson, M. D. Sammito, O. V Sobolev, D. H. Stockwell, T. C. Terwilliger, A. G. Urzhumtsev, L. L. Videau, C. J. Williams, P. D. Adams, *Acta Crystallogr. Sect. D* **2019**, *75*, 861–877.

[23] P. Emsley, K. Cowtan, *Acta Crystallogr. Sect. D Biol. Crystallogr.* **2004**, *60*, 2126–2132.

[24] P. V Afonine, B. K. Poon, R. J. Read, O. V Sobolev, T. C. Terwilliger, A. Urzhumtsev, P. D. Adams, *Acta Crystallogr. Sect. D* **2018**, *74*, 531–544.

[25] C. J. Williams, J. J. Headd, N. W. Moriarty, M. G. Prisant, L. L. Videau, L. N. Deis, V. Verma, D. A. Keedy, B. J. Hintze, V. B. Chen, S. Jain, S. M. Lewis, W. B. 3rd Arendall, J. Snoeyink, P. D. Adams, S. C. Lovell, J. S. Richardson, D. C. Richardson, *Protein Sci.* **2018**, *27*, 293–315.

[26] Schrödinger, LLC, *The {PyMOL} Molecular Graphics System, Version~1.8*, **2015**.